Mechanistic Contrasts between Manganese and Rhenium Bipyridine Electrocatalysts for the Reduction of Carbon Dioxide

Christoph Riplinger,[†] Matthew D. Sampson,[‖] Andrew M. Ritzmann,[‡] Clifford P. Kubiak,[‖] and Emily A. Carter*[†,§,⊥]

[†]Department of Mechanical and Aerospace Engineering, [‡]Department of Chemical and Biological Engineering, [§]Program in Applied and Computational Mathematics, and [⊥]Andlinger Center for Energy and the Environment, Princeton University, Princeton, New Jersey 08544-5263, United States

[‖]Department of Chemistry and Biochemistry, University of California, San Diego, La Jolla, California 92093-0358, United States

Ⓢ *Supporting Information*

ABSTRACT: $[Re(bpy)(CO)_3]^-$ is a well-established homogeneous electrocatalyst for the reduction of CO_2 to CO. Recently, substitution of the more abundant transition metal Mn for Re yielded a similarly active electrocatalyst, $[Mn(bpy)(CO)_3]^-$. Compared to the Re catalyst, this Mn catalyst operates at a lower applied reduction potential but requires the presence of a weak acid in the solution for catalytic activity. In this study, we employ quantum chemistry combined with continuum solvation and microkinetics to examine the mechanism of CO_2 reduction by

each catalyst. We use cyclic voltammetry experiments to determine the turnover frequencies of the Mn catalyst with phenol as the added weak acid. The computed turnover frequencies for both catalysts agree to within one order of magnitude of the experimental ones. The different operating potentials for these catalysts indicate that different reduction pathways may be favored during catalysis. We model two different pathways for both catalysts and find that, at their respective operating potentials, the Mn catalyst indeed is predicted to take a different reaction route than the Re catalyst. The Mn catalyst can access both catalytic pathways, depending on the applied potential, while the Re catalyst does not show this flexibility. Our microkinetics analysis predicts which intermediates should be observable during catalysis. These intermediates for the two catalyzed reactions have qualitatively different electronic configurations, depending on the applied potential. The observable intermediate at higher applied potentials possesses an unpaired electron and therefore should be EPR-active; however, the observable intermediate at lower applied potentials, accessible only for the Mn catalyst, is diamagnetic and therefore should be EPR-silent. The differences between both catalysts are rationalized on the basis of their electronic structure and different ligand binding affinities.
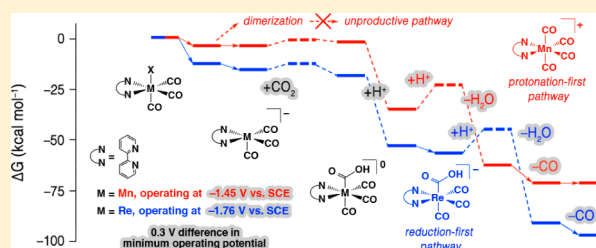
■ INTRODUCTION

In recent years, tremendous efforts have been made to develop alternative energy technologies exploiting a variety of renewable energy sources such as solar and wind energy. However, these two technologies produce electricity only intermittently; for either to contribute significantly in a renewable energy future requires some form of storage of excess electricity. Grid-scale storage does not exist yet, for a variety of reasons, only some of them technological.[1] The technology conundrum for electrochemical energy storage, in particular, is illustrated by the following trade-off: batteries have a high energy density but limited lifetime, while supercapacitors have long lifetime but low energy density.[2] Therefore, other forms of storing electrical energy also need to be explored and optimized. One solution to this problem is to convert electrical energy into chemical energy, which then can be utilized on demand to drive an engine or produce electricity in a fuel cell. Using carbon dioxide (CO_2) as a substrate in this type of conversion is attractive because it renders the fuel cycle carbon-neutral. Reduction of CO_2 to fuels or fuel precursors, such as carbon monoxide (CO), methanol, or longer chain alcohols, is possible.[3,4] The

latter possess relatively high energy densities and are liquids under standard conditions, facilitating their transport and storage. In a laboratory setting, several synthetic catalytic systems have been established for CO_2 reduction, as described in a variety of recent reviews.[5−14] A first step in this process could involve (photo)electrochemically reducing CO_2 to CO using energy generated from a photoexcitation in a semiconductor or from an applied external voltage, where the latter could originate from a renewable source, such as wind turbines or photovoltaics.[15]

Of the systems that electrochemically reduce CO_2 to CO, *fac*-Re(bpy)(CO)$_3$Cl (bpy = 2,2′-bipyridine) and its synthetic analogues are superior to most others in terms of rates, selectivities, and lifetimes.[15−18] (Since all of the metal bpy complexes discussed in this study are *fac*-, this label will henceforth be omitted.) The properties of these Re catalysts have been the subject of exhaustive experimental and computational investigations.[15−26] These catalysts operate in

organic solvents (e.g., acetonitrile, MeCN) and reduce CO_2 with and without explicitly adding an external proton (H^+) source to the solution. A variety of substituents at the 4,4'-positions of the bpy ligand have been shown to be active, and the catalyst operates at a potential of −1.7 to −2.0 V relative to the saturated calomel electrode (SCE), depending on the substitution of the bpy ligand.[13,16,17] The active catalyst, doubly reduced $[Re(bpy)(CO)_3]^-$, has a singlet ground state and possesses a formal charge distribution of $Re^0(bpy)^{-}$.[26] This ground state places one electron (formally) in a bpy π^* orbital and the other electron in a Re d_{z^2} orbital. This unique electronic configuration favorably interacts with CO_2, exhibiting a lower activation barrier for CO_2 binding compared to H^+ binding, resulting in a remarkable selectivity for CO_2 reduction over H^+ reduction.[15,22]

Second- and third-row transition metals have long been the benchmarks for reductive catalysis due to superior activities and stabilities when compared to their first-row counterparts. These transition metals are very expensive due to their scarcity in the Earth's crust; therefore, they are not ideal for use on an industrial scale. Mn is approximately 1.3 million times more abundant[27] in the Earth's crust than Re and therefore is much more promising for practical scale-up. Bourrez et al. in 2011 and Smieja et al. in 2013 both utilized Mn as a substitute for Re in metal bpy electrocatalysts.[20,28] Prior to these reports, Johnson et al. originally reported that the doubly reduced $[Mn(bpy)(CO)_3]^-$ anion (analogous to the active Re catalyst) does not react with CO_2,[25] and therefore, these Mn catalysts were not pursued for CO_2 reduction electrocatalysis for some time. Bourrez et al. discovered that these Mn catalysts require the addition of weak Brønsted acids to exhibit CO_2 reactivity and, thus, to exhibit catalytic turnover in electrocatalysis. The corresponding Re catalysts, however, operate without the necessity of an external H^+ source,[20] although the addition of weak Brønsted acids significantly increases catalytic rates.[15,18] Other than the difference in Brønsted acid dependence, the Mn and Re catalyst systems possess two other key differences worth noting. $Mn(bpy)(CO)_3Br$ and its synthetic analogues reduce CO_2 to CO at a lower applied potential than the corresponding Re catalysts, without sacrificing much activity.[20] The Mn catalysts rapidly lose Br^- and dimerize after a single-electron reduction, whereas the corresponding Re catalysts do not lose Cl^- until either a second one-electron reduction occurs or a slow ligand-to-metal charge transfer (LMCT) occurs.[16,20] Since the Mn catalysts offer the potential for eventual scale-up and industrial use, recent work has focused on elucidating catalytic differences between the two systems in order to optimize the Mn catalysts' properties.[23,29,30]

In this work, we compare the complete electrocatalytic cycles of both the Mn and Re catalysts. We employ hybrid density functional theory (DFT) + continuum solvation calculations in order to optimize the geometries of the different reaction intermediates and transition states. We calculate the reduction potentials, reaction free energies, and activation barriers for the individual reaction steps, and use these data to perform microkinetics simulations of the catalytic reaction course. These simulations help us to identify the rate-limiting steps for each catalytic cycle, which then helps us understand key differences in behavior between the two catalysts.

■ METHODS

Computational Methodology. All quantum chemical calculations were performed using the ORCA program package.[31] The geometry optimizations were performed using DFT with the B3LYP[32–34] exchange-correlation functional, employing the "resolution of the identity" approximation for the evaluation of the Coulomb matrices and a seminumeric exchange treatment via the "chain-of-spheres" algorithm for forming the exchange-type matrices (RIJCOSX).[35] The def2-SVP basis set was used along with the corresponding def2-SVP/J auxiliary basis set[36,37] (denoted B1), with LANL effective core potentials (ECPs) and the LANLDZ basis sets for Mn, Re, K, Br, and Cl (10 core electrons each of Mn, K, and Cl, 28 core electrons of Br, and 60 core electrons of Re are subsumed into the ECPs).[38] Single-point energy calculations on the optimized geometries were carried out with DFT-B3LYP using the aug-cc-pVTZ basis set[39] for all atoms except for Mn, Re, K, Br, and Cl, where LANL ECPs and the LANLDZ basis sets were used (denoted B2). In all calculations, the D3 dispersion correction of Grimme et al. was applied.[40] The solvent MeCN was modeled as a dielectric continuum (ε = 36.6, refractive index = 1.334) using a conductor-like screening model (COSMO).[41] All stationary structures were characterized by vibrational frequency calculations, using the same level of theory as for the geometry optimizations. Thermochemical contributions were calculated using the ideal gas, rigid rotor, and harmonic oscillator approximations at a temperature of 298.15 K. An appropriate scaling factor of 0.9614 was used for the vibrational frequencies.[42] Calculated values were corrected by $\Delta G^{0\rightarrow*}$ = 1.89 kcal/mol for the change in standard states from gas phase to condensed phase.[43]

The total Gibbs free energy (G) was computed as

$$G = E_{gas}^{B3LYP,B2} + (G - E)_{gas}^{B3LYP,B1} + (E_{solv}^{B3LYP,COSMO,B2}$$
$$- E_{gas}^{B3LYP,B2}) + \Delta G^{0\rightarrow*} \tag{1}$$

with subscripts indicating if the geometry was optimized in gas phase or using COSMO. The superscripts in eq 1 describe the applied level of theory. Here, E is the single-point energy, $(G - E)_{gas}^{B3LYP,B1}$ incorporates the thermochemical and entropic corrections calculated at the geometry optimization level of theory, and $E_{solv}^{B3LYP,COSMO,B2} - E_{gas}^{B3LYP,B2}$ adds in the solvation energy. We model an applied potential, Φ, by adding $-e\Phi$ for each added electron. We use the explicit solvation energy of a proton in MeCN (-260.2 kcal/mol)[22,44] for the reaction free energy calculations and a phenol molecule as an explicit proton source for the barrier calculations.

Refinement of Activation Barriers. Activation barriers were also computed using DLPNO-CCSD(T) (only closed-shell systems) and LPNO-CCSD (both closed-shell and open-shell systems).[45–47] For these single-point calculations, the minimally augmented def2-SVP and def2-TZVPP basis sets were used for all atoms,[37,48] with corresponding segmented all-electron relativistically recontracted basis sets for Mn and Re.[49] We used the two-point extrapolation scheme by Truhlar with extrapolation parameters α = 3.4 and β = 2.4 to obtain the activation barriers at the complete basis set limit.[50] The zeroth-order regular approximation (ZORA) was applied for the treatment of scalar relativistic effects.[51,52] For calculations of refined Gibbs free energies, $E_{gas}^{B3LYP,B2}$ was substituted by $E_{gas}^{LPNO-CCSD/DLPNO-CCSD(T),B3}$.

Reduction Potentials. Standard reduction potentials were calculated following the methodology in ref 22. As described there, we used K^+ as a counterion for those complexes for which a small anion (Cl^- or Br^-) is involved in the reduction reaction. All reported reduction potentials are referenced to the SCE, which has an absolute potential of -4.422 V in MeCN.[53]

Rate Constants. Bimolecular rate constants were computed using classical transition state theory,[54,55] calculated as follows:

$$k = \frac{k_B T}{h} \cdot K^0 \cdot \exp\left(\frac{-\Delta G^{\ddagger,0}}{RT}\right) \tag{2}$$

where k is the rate constant, k_B is the Boltzmann constant, T is the temperature, h is Planck's constant, K^0 is the inverse of the standard state concentration (1 M), R is the universal gas constant, and $\Delta G^{\ddagger,0}$ is the standard free energy of activation (obtained at the standard state of 1 M, 298.15 K, and 1 atm for all species).

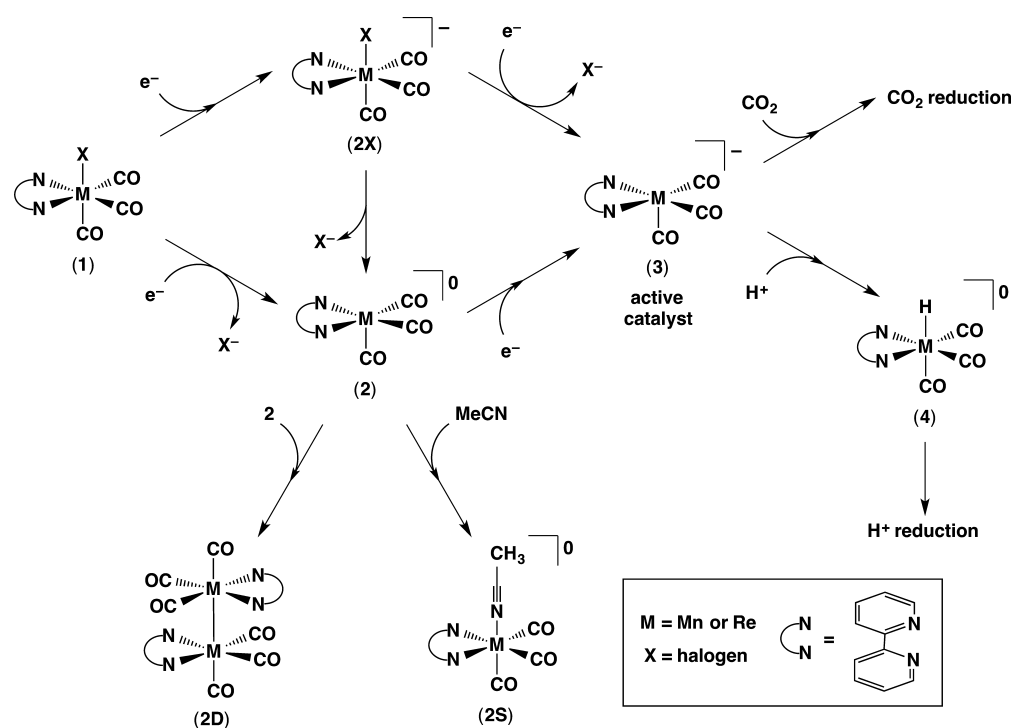**Figure 1.** Overview of the possible products after one- and two-electron reductions of $Mn(bpy)(CO)_3Br$ (**1-Mn**) and $Re(bpy)(CO)_3Cl$ (**1-Re**).

Microkinetics Simulations. Microkinetics simulations were based on the reaction mechanism proposed by Keith et al.[22] This mechanism contains two types of steps: reduction steps and chemical steps. The chemical steps involve no electron addition/removal. We employ rate constants obtained from classical transition state theory (vide supra) for these reactions. We assume that the reduction steps are much faster than the chemical steps such that the reduction reactions are in equilibrium at all times. The equilibrium constants were computed from the standard relationship: $K = \exp(-\Delta G^\circ/RT)$, where ΔG° is the reaction free energy at the standard temperature and concentration but adjusted to account for the applied potential (vide supra).

Our microkinetics simulations were performed using MATLAB. We employed a time step of 1 ps to ensure that the integration gave appropriate concentration profiles. We assumed that a quasi-equilibrium exists for all reduction steps at all times (i.e., all reduction steps are fast relative to the chemical steps). This allowed us to decompose each time step into three parts: (1) equilibrating the reduction steps given the instantaneous concentrations, (2) computing the reaction rates for the chemical steps using the concentrations obtained after equilibrating the reduction steps, and (3) propagating the system forward in time using the computed rates for the chemical steps. The chemical steps act as barriers during equilibration, giving rise to three subgroups that are equilibrated separately. We solved each of the equilibrium problems using the Newton−Raphson method with the Jacobian matrix explicitly computed for the appropriate reaction subgroup. Highly negative potentials (e.g., −2.0 V vs SCE) led to poorly conditioned Jacobian matrices, due to large equilibrium constants. In cases where the poor conditioning led to convergence failure, we scaled back the largest equilibrium constants by four orders of magnitude (i.e., from $O(10^{11})$ to $O(10^7)$) in order to restore proper convergence behavior. Scaling the equilibrium constants in this manner should have very little impact on the overall equilibrium because the resulting equilibrium constants still drive the corresponding reactions to completion. The time-dependent concentrations of the various species (in M) were obtained using Euler's method for integration. The initial simulation conditions were chosen similar to the experimental conditions, namely, 1 mM catalyst concentration, 0.3 M CO_2 concentration (concentration of saturated CO_2 in MeCN),[18] 0.57 M phenol in the simulations with the Re complex, and 0.21 M with the Mn complex.

Experimental Methodology. Electrochemical experiments were performed using a BASi Epsilon potentiostat. A single-compartment cell was used for all cyclic voltammetry experiments with a glassy carbon working electrode (3 mm in diameter from BASi), a Pt wire counter electrode (flame annealed with butane torch), and a Ag/AgCl pseudoreference. Ferrocene (Fc) was added as an internal reference. All electrochemical experiments were performed with 0.1 M tetrabutylammonium hexafluorophosphate (TBAPF$_6$) as the supporting electrolyte. Electrochemical cells were shielded from light during experiments. All solutions were purged with nitrogen (N_2) or CO_2 before cyclic voltammograms (CVs) were taken. "Bone dry" CO_2 run through a Drierite column was used for all relevant electrochemistry experiments. Experiments with CO_2 were performed at gas saturation (∼0.3 M) in MeCN. All potentials were referenced vs SCE by adding 380 mV to an internal Fc$^+$/Fc couple.[56] Mn(bpy)(CO)$_3$Br was synthesized following known literature procedures.[20,28] MeCN solvent was purged with argon, dried on a custom dry solvent system over alumina columns, and stored over molecular sieves before use. TBAPF$_6$ (Aldrich, 98%) was twice recrystallized from methanol (MeOH) and dried under a vacuum at 90 °C overnight before use. Phenol was purchased from Alfa Aesar (detached crystals, 99+%) and used as received.

RESULTS AND DISCUSSION

Dimerization. Previous experimental work has shown that a single-electron reduction of Re(bpy)(CO)$_3$Cl (**1-Re**) in MeCN is primarily bpy ligand-based, forming the six-coordinate anion **2X-Re** (Figure 1). This reduction is followed by a LMCT, resulting in loss of Cl$^-$ and formation of a five-coordinate Re^0 complex (**2-Re**, Figure 1). The five-coordinate complex **2-Re** can then react with itself to form a Re^0−Re^0 dimer (**2D-Re**, Figure 1).[16,57] This dimer is expected to show little to no activity, as a similar dimer with dimethyl-substituted bpy ligands was reported to be unreactive toward CO_2.[58] In contrast to Re, Mn(bpy)(CO)$_3$Br (**1-Mn**) more readily dimerizes after the first reduction, with no evidence for singly reduced monomers (**2X-Mn** or **2-Mn**) in in situ electrochemical studies.[20,28] Dimerization has been shown to detrimentally increase the

overpotential to form the two-electron-reduced, catalytically active complex **3-Mn**.[29] Recently, the Mn^0-Mn^0 dimer (**2D-Mn**) has been shown to be catalytically active, photochemically reducing CO_2 to formic acid.[59,60] When the bpy ligand of dimer **2D-Mn** is substituted with electron-donating groups, such as methyl groups, it also displays electrocatalytic activity, reducing CO_2 to CO.[30] However, the rates for these catalytic reactions are assumed to be much slower than the electrocatalytic reduction of CO_2 to CO by **3-Mn**.

In our first set of analyses for the Mn and Re catalysts, we investigated the free energies for possible reaction pathways of the catalyst precursors. These possible pathways are depicted in Figure 1. For both Mn and Re, the one-electron-reduced species is formed through reduction of **1-Mn** and **1-Re**. After one-electron reduction, the halide ion (X^-) can remain bound to the metal center (**2X**) or can dissociate (**2**). Upon a second one-electron reduction, these singly reduced complexes form the active catalyst **3**. Before the second reduction, five-coordinate complex **2** can either dimerize with itself to yield the M^0-M^0 dimer **2D** or bind a MeCN solvent molecule to form six-coordinate, neutral **2S**. The computed reduction potentials and reaction free energies for these aforementioned reactions are summarized in Tables 1 and 2. As can be seen

Table 1. Computed One-Electron Reduction Potentials (V vs SCE) for the First Two Reductions of $Mn(bpy)(CO)Br$ (1-Mn) and $Re(bpy)(CO)_3Cl$ (1-Re)^a

reduction	potential (Mn catalyst)	potential (Re catalyst)
1 → 2X	−1.41	−1.23^d
1 → 2	−1.27^b	−1.59
2X → 3	−1.27	−1.76^e
2 → 3	−1.45^c	−1.25

^{a}See Figure 1. All values are given for standard states at room temperature. ^{b}Experimental reduction potential of **1-Mn** → **2-Mn** = −1.26 V vs SCE.[28] ^{c}Experimental reduction potential of **2-Mn** → **3-Mn** = −1.50 V vs SCE.[28] ^{d}Experimental reduction potential of **1-Re** → **2X-Re** = −1.34 V vs SCE.[16] ^{e}Experimental reduction potential of **2X-Re** → **3-Re** = −1.73 V vs SCE.[16]

Table 2. Reaction Free Energies (kcal/mol) for the Interconversion of One-Electron-Reduced $[Mn(bpy)(CO)_3Br]^-$ (2X-Mn) and $[Re(bpy)(CO)_3Cl]^-$ (2X-Re) Complexes^a

reaction	ΔG (Mn catalyst)	ΔG (Re catalyst)
2X → 2	−4.7	7.7
2 → 2S	6.1	−6.0
2 → 2D	−20.3^b	−37.2^b

^{a}See Figure 1. All values are given for standard states at room temperature. ^{b}The cc-pVTZ basis set was used because of SCF convergence problems instead of aug-cc-pVTZ as used for the other reactions.

from Table 1, the computed reduction potentials are in very good agreement with the experimental values. We predict that the preferred pathway for the Re catalyst is reduction of **1-Re** to **2X-Re**, which then loses its Cl^- ligand upon the second reduction. The pathway for the Mn complex is predicted to be different. **1-Mn** is preferentially reduced to **2-Mn**, concomitantly losing the Br^- ligand. **2-Mn** is then further reduced to **3-Mn**. We discuss the different stabilities of the singly reduced species in more detail below. Note that the first reduction step has a similar reduction potential for both catalysts, whereas the

second reduction step has a much more negative reduction potential for Re, consistent with the required operating potentials found in experiments.

Of the three possible monomeric, one-electron-reduced Re complexes (Table 2), the five-coordinate structure, **2-Re**, is predicted to be the least stable. In MeCN, the singly reduced, monomeric Re complex is most stable with a bound halide ion (**2X-Re**). Removal of the Cl^- ligand from singly reduced **2X-Re** is predicted to be endergonic by ~8 kcal/mol. The Re–Cl complex **2X-Re** is also found to be more stable than the Re–MeCN complex **2S-Re** by 1.7 kcal/mol. These predictions are consistent with experimental electron paramagnetic resonance (EPR) data showing that singly reduced **2X-Re** is stable in MeCN.[61]

The reaction free energies of the monomeric, one-electron-reduced Mn complexes are significantly different from their Re counterparts. The singly reduced, five-coordinate complex **2-Mn** is more stable than the singly reduced Mn complexes with a bound sixth ligand, either Br^- (**2X-Mn**) or MeCN (**2S-Mn**). This stability is in agreement with recent time-resolved infrared spectroscopy experiments on $Mn(bpy-tBu)(CO)_3Br$ (bpy-*t*Bu = 4,4′-di-*tert*-butyl-2,2′-bipyridine) from Grills et al., who measured a radical–radical recombination rate that is many orders of magnitude greater than that of typical solvent-coordinated metal complexes, such as that measured for $[Re(bpy)(CO)_3(THF)]^0$ by Fujita and Muckerman ($2k = 1.3 \times 10^9$ M^{-1} s^{-1} and $2k = 40$ M^{-1} s^{-1} for Mn and Re, respectively).[59,62] The singly reduced, five-coordinate Mn complex **2-Mn** is therefore predicted to be available for the observed very fast radical–radical recombination to form dimer **2D-Mn**. Similar to Fujita and Muckerman, we can estimate the relative dimerization rates for the monomeric, one-electron-reduced Re and Mn complexes.[62] Comparing the fractions of five-coordinate complexes that are available for dimerization (and assuming that the barriers for dimerization are similar for both species), we conclude that the initial rate of dimerization for **2-Re** is about 10^9 times slower than the dimerization rate for **2-Mn** (see Supporting Information), similar to the experimental comparison made above.

As expected, for both Mn and Re, the negatively charged halide ions (in **2X**) bind more strongly to the metals than the MeCN solvent molecule (in **2S**). Here, the important difference between Mn and Re is that the five-coordinate Mn^0 complex **2-Mn** is more stable than the MeCN-coordinated complex **2S-Mn**; however, for Re, the opposite is true. The MeCN-coordinated Re^0 complex **2S-Re** is more stable than five-coordinate **2-Re**. Taking **2S** as a reference, the five-coordinate Mn^0 complex **2-Mn** is approximately 12 kcal/mol more stable than the five-coordinate Re^0 complex **2-Re**. Since Mn is a first-row transition metal, its $3d_{z^2}$ orbital is expected to be lower in energy than the bpy π^* orbital, favoring a metal-based reduction before a bpy-based reduction.[23] By contrast, Re is a third-row transition metal and therefore the bpy π^* orbital is expected to be lower in energy than the Re $5d_{z^2}$ orbital, favoring a bpy-based reduction before a metal-based reduction. This trend can be verified by comparing the Mulliken spin populations for the singly reduced Mn and Re complexes. Singly reduced **2X** has approximately zero spin population on the metal center for both Mn and Re. For singly reduced **2**, the Mn center possesses twice as much net α spin population as the Re center (Mn = 0.47 and Re = 0.25 α spin population, respectively). The three CO ligands carry only a small amount of α spin population in each case, with the majority of the
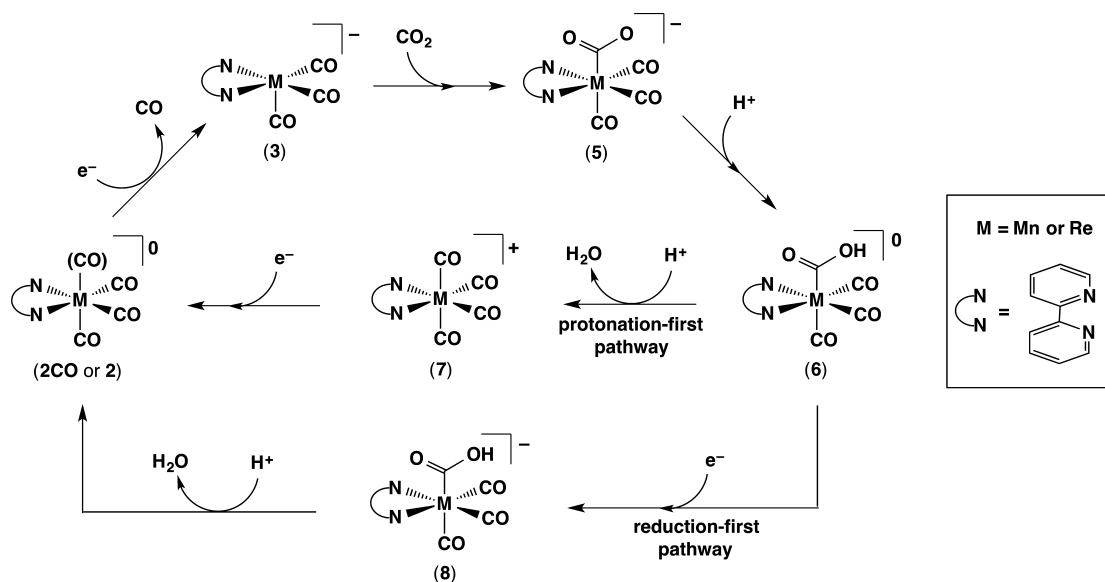
Figure 2. Schematic catalytic reaction mechanism of CO_2 reduction by the active catalysts $[Mn(bpy)(CO)_3]^-$ (**3-Mn**) and $[Re(bpy)(CO)_3]^-$ (**3-Re**).

remaining α spin population residing on the bpy ligand. Occupation of the 3d orbital on Mn in **2-Mn** disfavors binding a ligand to the sixth coordination site because of Pauli repulsion, while the much lower occupation of the 5d orbital on Re in **2-Re** allows binding of a sixth ligand to occur.

These computed properties can be compared to experimental results of a spectroelectrochemical study of $[M(iPr\text{-}DAB)(CO)_3]^-$ (M = Mn or Re, iPr-DAB = isopropyl diazabutadiene), where the iPr-DAB ligand possesses a comparable π^* orbital as the bpy ligand.[63,64] For this five-coordinate species with an iPr-DAB ligand, the electron density on Mn is higher than on Re, consistent with the observed trend between **2-Mn** and **2-Re** in our study. In order to test the role of the bpy ligand in these singly reduced complexes, we substituted it with two CO ligands and calculated the binding affinity of Br^- and Cl^- to $[Re(CO)_5]^0$ and $[Mn(CO)_5]^0$ fragments (see Table S1 in the Supporting Information). Indeed, binding of Br^- and Cl^- to these pentacarbonyl complexes is predicted to be endergonic by ~2 kcal/mol in both cases. This shows that the bpy ligand is responsible for the differences in ligand binding affinities for **2-Mn** and **2-Re**. Upon binding of the sixth ligand, the spin density in the d_{z^2} orbital is pushed onto the bpy ligand, which is energetically more costly in the case of **2-Mn** since the bpy π^* orbital is higher in energy than the Mn d_{z^2} orbital, as discussed above. In summary, the difference in ligand binding affinities is primarily due to the relative energy differences of the bpy π^* orbital and the metal d_{z^2} orbitals and their subsequent occupations upon reduction.

Catalyst Selectivity. Experimentally, both the Mn and Re catalysts (**3**) have been shown to exhibit a remarkable selectivity toward CO_2 reduction over H^+ reduction.[15,28] For the Re catalyst, our group recently showed that this selectivity originates from a much higher barrier to protonate the active catalyst **3-Re** (to yield **4-Re**, see Figure 1), as compared to the barrier for CO_2 binding to **3-Re** (to yield **5-Re**, see Figure 2).[22] In this work, we investigate H^+ and CO_2 binding to the active Mn catalyst **3-Mn** and compare the results to those of active Re catalyst **3-Re**. Since our methodology differs (in the choice of the Brønsted acid and the inclusion of a dispersion correction) from the one used previously for the Re catalyst,[22] a fair

comparison requires that we report new computed values for both Mn and Re. The reaction barriers and reaction free energies are summarized in Table 3.

Table 3. Reaction Free Energies and Activation Barriers (kcal/mol) for CO_2 Binding and H^+ Binding to the Active Catalysts 3-Mn and 3-Re[a]

reaction	Mn catalyst	Re catalyst
$\Delta G\ddagger$ (3 → 4)	13.4	12.8
ΔG (3 → 4)	−37.5	−42.7
$\Delta G\ddagger$ (3 → 5)	3.3	3.2
ΔG (3 → 5)	2.2	−3.4
$\Delta G\ddagger$ (5 → 6)	barrierless	barrierless
ΔG (5 → 6)	−33.4	−34.0

[a]See Figure 3. The barriers were calculated with DFT-B3LYP using basis set B2. All values are given for standard states at room temperature.

For both catalysts, the reaction barriers for protonation of **3** are ~10 kcal/mol higher than the barriers for CO_2 addition to **3** (as also illustrated in Figure 3). Surprisingly, the barriers for protonation, as well as the barriers for CO_2 addition, are very similar for both catalysts; this indicates either that both metal centers behave very similarly in these reactions or that the influence of the metal center on the reaction barriers is negligible. The latter of these two explanations then raises the question: what is the origin of the reaction barrier heights? We discuss this question in more detail below. In the previously reported calculations on the Re catalyst,[22] stronger Brønsted acids were found to lower the reaction barrier for protonation of **3-Re**. It was further suggested that H_2 evolution becomes favorable over CO_2 reduction if the Brønsted acid is strong enough, e.g., with HCl (with a calculated pK_a of 11 in MeCN). Since the barrier heights for protonation are identical for both catalysts in our study, we expect this threshold pK_a to be very similar for both catalysts.

Electrocatalytic CO_2 Reduction Cycle. The overall catalytic cycle for CO_2 reduction for each catalyst is outlined in Figure 2. The catalytic cycle is initiated by CO_2 binding to
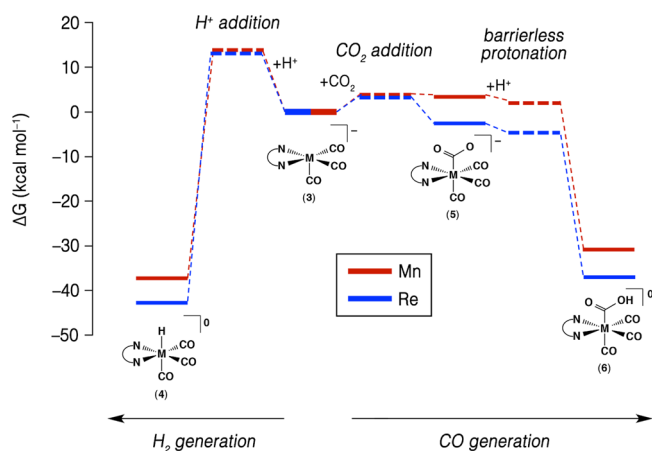
Figure 3. Potential energy surface for H^+ or CO_2 addition to active catalysts **3-Mn** and **3-Re**. Reaction intermediates are depicted with solid lines and transition states are depicted with dashed lines. Corresponding numerical values are given in Table 3.

the metal center of **3**, and subsequent protonation of the bound CO_2 ligand (**5 → 6**) leads to a hydroxycarbonyl complex. The mechanism can then proceed via two different pathways: (i) reduction followed by protonation (reduction-first pathway, via **8**) or (ii) protonation followed by reduction (protonation-first pathway, via **7**). In the reduction-first pathway, **6** is reduced to **8**, which undergoes C−OH bond cleavage initiated by protonation of the OH to form water and **2CO**. In the protonation-first pathway, protonation of **6** results in C−OH bond cleavage and formation of water and the cationic tetracarbonyl complex **7**, which generates **2CO** upon reduction. In each pathway, the CO ligand can either (i) spontaneously dissociate from **2CO** to form **2**, which then is reduced to regenerate active catalyst **3**; or (ii) remain bound to the metal center until the second reduction step (**2CO → 3**), whereupon CO is released and active catalyst **3** is regenerated. In considering possible catalytic intermediates, only mononuclear species, i.e., no dimers of any type, were considered because the experimental catalytic reaction order is known to be first-order in each catalyst.[18,20,29] In the following theoretical calculations, we analyze the thermodynamic and kinetic properties of the catalytic cycle, as well as the structural and electronic changes of each mechanistic step.

We stated above that the reaction barriers for CO_2 addition to **3-Mn** and **3-Re** are very similar. However, the reaction free energies for CO_2 addition are quite different for each catalyst (Table 3). CO_2 addition to **3**, as well as protonation of **3**, is 5−6 kcal/mol less favored for the Mn catalyst compared to the Re catalyst. Binding of CO_2 to **3-Re** is slightly exergonic, whereas binding of CO_2 to **3-Mn** is slightly endergonic. For the Mn catalyst, only the subsequent reaction step protonating the CO_2 adduct in **5-Mn** stabilizes the ligand (to yield **6**) and thermodynamically drives CO_2 binding to the Mn center (as illustrated in Figure 3). The formation of **6-Mn** via protonation of **5-Mn** is thus critically dependent on the availability of H^+ in solution. As mentioned earlier, without added weak Brønsted acid, CO_2 does not bind to the Mn center in **3-Mn**; however, with available weak acid in solution, CO_2 binding is observed.[29] Our free energy calculations and these experimental results thus explain the necessity of added weak acid for CO_2 reduction by the Mn catalyst.[20,29] On the other hand, Re catalyst **3-Re** reduces CO_2 experimentally without an external H^+ source;

however, rates are greatly increased by the addition of weak Brønsted acids. This activity in the absence of H^+ is thought to arise partly from the high overpotentials needed to access the active catalyst **3-Re**.[15] Under these experimental conditions, the Re catalyst can strip H^+ from MeCN solvent[65] or from the supporting electrolyte via Hofmann degradation.[66] Both catalysts show similar dependence of their turnover frequencies on the addition of weak acid.[15,18,20,29]

As described above, after protonation of the CO_2 adduct to form **6**, there are two possible pathways for the reaction mechanism to proceed, either by a reduction-first or a protonation-first pathway (via generation of **8** or **7**, respectively). For both pathways, protonation of the OH group destabilizes the C−O bond, resulting in heterolytic C−O bond cleavage, which produces CO and releases one H_2O molecule. Table 4 summarizes the reduction potentials for both

Table 4. Computed One-Electron Reduction Potentials (V vs SCE) for the Reduction Steps in the Mn and Re Catalytic Cycle[a]

reduction	potential (Mn catalyst)	potential (Re catalyst)
6 → 8	−1.69	−1.56
7 → 2CO	−1.30	−1.17[c]
7 → 2 + CO	−1.26	−1.64
2CO → 3 + CO	−1.41	−1.67
2 → 3	−1.45[b]	−1.21
2S → 3 + MeCN	−1.18	−1.51[d]

[a]See Figures 4 and 5. All values are given for standard states at room temperature. [b]Experimental reduction potential for **2-Mn → 3-Mn** = −1.50 V vs SCE.[28] [c]Experimental reduction potential for **7-Re → 2CO-Re** = −1.15 V vs SCE.[21] [d]Experimental reduction potential for **2S−Re → 3-Re** = −1.42 V vs SCE.[21]

the reduction-first and protonation-first pathways, which are in excellent agreement with the available experimental data, and Table 5 summarizes the calculated reaction free energies and activation barriers for the C−O bond cleavage steps in both pathways.

Table 5. Reaction Free Energies and Activation Barriers (kcal/mol) for C−O Bond Cleavage of Neutral and Reduced [Mn(bpy)(CO)$_3$COOH]$^{0/-}$ (6-Mn and 8-Mn) and [Re(bpy)(CO)$_3$COOH]$^{0/-}$ (6-Re and 8-Re)[a]

reaction	Mn catalyst	Re catalyst
$\Delta G\ddagger$ (**6 → 7**)	11.9	11.9
ΔG (**6 → 7**)	−27.8	−24.6
$\Delta G\ddagger$ (**8 → 2CO**)	11.9	11.6
ΔG (**8 → 2CO**)	−36.7	−33.5

[a]See Figure 4. The barriers were calculated with DFT-B3LYP using basis set B2. All values are given for standard states at room temperature.

In order to simplify our discussion of the reaction free energies and activation barriers for these two pathways, we first discuss the two pathways for the Re catalytic cycle and then directly compare the results with those for the Mn catalytic cycle. The activation barriers for C−O bond cleavage in each pathway for the Re system are almost identical; however, the reaction free energies for the reduction steps in each pathway differ significantly (Table 5). Thermodynamically, reduction of **6-Re** to generate **8-Re** is approximately 9 kcal/mol more costly
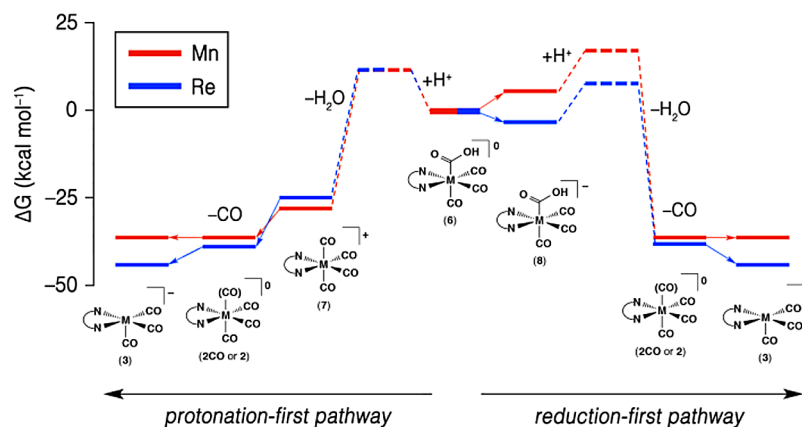
Figure 4. Potential energy surface for reduction- and protonation-initiated C–O bond cleavage of the protonated M–CO$_2$ adduct (**6**). Shown are the two accessible pathways, a protonation-first pathway (protonation of **6**, followed by reduction of **7**; left scheme) and a reduction-first pathway (reduction of **6**, followed by protonation of **8**; right scheme). Reaction intermediates are depicted with solid lines, transition states with dashed lines. Arrows indicate electron transfer steps. These calculations are performed with applied potentials of −1.45 and −1.76 V vs SCE for Mn and Re, respectively; see text for further explanation.
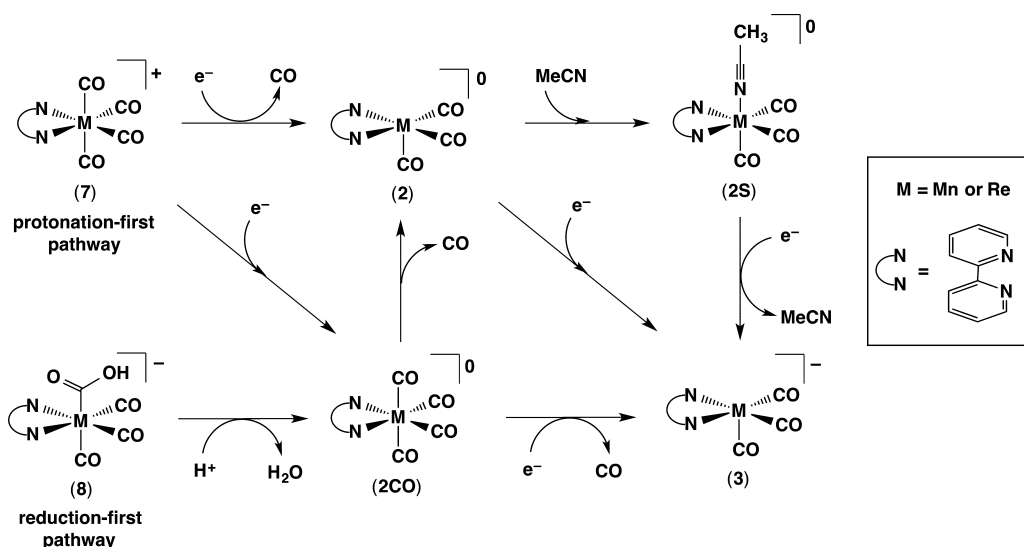

Figure 5. Overview of possible products after C–O bond cleavage in the Mn and Re catalytic cycles.

compared to reduction of **7-Re** to generate **2CO-Re** (Table 4). This thermodynamic difference is easily rationalized by the presence of the positive charge on **7-Re** that produces an increased electron affinity compared to neutral **6-Re**. The activation barriers for C–O bond cleavage are the largest barriers in the catalytic cycle. As the two pathways (reduction-first and protonation-first) each contain a C–O bond cleavage step, we can expect that only one of the preceding intermediates, **6** or **8**, will accumulate in a microkinetics cycle if only one pathway is taken. A mixture of **6** and **8** can be expected if both pathways are accessible, and the preferred reaction channel will depend strongly on the equilibrium between **6** and **8**.

The activation barriers and reaction free energies in the Mn catalytic cycle show similar trends to those in the Re catalytic cycle. Interestingly, the C–O bond cleavage barriers of **6-Mn** and **8-Mn** are almost identical to those of the corresponding Re intermediates (Table 5). The largest difference between the two catalytic cycles arises in the electron affinities, where the reactions **6 → 8** and **7 → 2CO** have about 0.1 V more negative reduction potentials for Mn as compared to Re (Table 4). This

difference suggests that a more negative potential is needed for the Mn catalyst in order to reduce CO$_2$, in contradiction to experimental observations. However, as will become clear with our microkinetics analysis (vide infra), the Mn catalyst has access to different catalytic pathways due to differences in ligand binding affinity and thus can be reduced at a less negative potential. This outcome emerges when we take into account reaction **7 → 2** + CO. Here, the reduction potential of the Mn intermediate is about 0.4 V less negative than for the corresponding Re intermediate (Table 4).

Figure 4 shows a comparison of both the reduction-first and protonation-first pathways for each catalyst, assuming that the applied potential is the minimum operating potential, i.e., the potential at which all the reduction reactions, via at least one of the pathways, are thermodynamically downhill (−1.45 and −1.76 V vs SCE for Mn and Re, respectively). It is reasonable to assume that interconversion of species **6** and **8** (reduction step) is much more rapid than the C–O bond cleavage steps, i.e., **6 → 7** and **8 → 2CO**. The ratio of **6** to **8** is determined by the potential-dependent thermodynamic equilibrium. For the Mn catalyst at its minimum operating potential, **6-Mn** is 5.5

kcal/mol more stable than **8-Mn** (Figure 4 and Table 4; ~10 800-fold higher concentration at room temperature). However, for the Re catalyst, **8-Re** is 4.6 kcal/mol more stable than **6-Re** (Figure 4 and Table 4; ~2400-fold higher concentration at room temperature). Given the similarity of reaction barriers (**6** → **7** and **8** → **2CO**; Table 5), we conclude that, at their respective minimum operating potentials, the Mn catalyst prefers the protonation-first pathway, whereas the Re catalyst prefers the reduction-first pathway, as previously suggested by Keith et al.[22] We further investigate this catalytic reaction pathway preference below.

After C−O bond cleavage and release of H_2O, there are three possible fates for the remaining CO ligand in **2CO**: (i) CO can stay coordinated to the metal center before further reduction occurs; (ii) CO can be substituted by a MeCN ligand to form **2S**, which has been experimentally observed for **2CO-Re**;[21] or (iii) CO can be spontaneously released to form **2**. These possible reaction pathways for **2CO** are shown in Figure 5. The reduction potentials and ligand binding affinities for these various species are summarized in Tables 4 and 6. As expected,

Table 6. Reaction Free Energies (kcal/mol) for the Interconversion of Neutral [Mn(bpy)(CO)₄]⁰ (2CO-Mn) and [Re(bpy)(CO)₄]⁰ (2CO-Re)^a

reaction	ΔG (Mn catalyst)	ΔG (Re catalyst)
2CO → **2** + CO	−0.9	9.8
2CO → **2** + CO^b	−3.8	6.9
2CO → **2** + CO^c	−5.0	5.7
2 + MeCN → **2S**	6.1	−6.0
2CO + MeCN → **2S** + CO	5.2	3.8
2CO + MeCN → **2S** + CO^b	2.3	0.9
2CO + MeCN → **2S** + CO^c	1.1	−0.3
2CO + MeCN → **2S** + CO^d	−0.4	−1.8

^{a}All values are given for standard states at room temperature, except where otherwise indicated. ^{b}[CO] = 8 mM. ^{c}[CO] = 1 mM. ^{d}[CO] = 0.08 mM.

the behavior of the intermediates in the reaction pathway of **2CO** is similar to the behavior of the singly reduced catalyst precursors that we have previously described. For the neutral Re complex, coordination of six ligands is favorable (**2CO-Re** or **2S−Re**), while the singly reduced Mn complex is most stable as a five-coordinate neutral complex **2-Mn**. For both

intermediates, CO binding is favored over binding of MeCN under standard conditions. However, in situ experiments have shown that the Re intermediate **2CO-Re** undergoes electron-transfer-catalyzed ligand substitution in MeCN, exchanging an axial CO ligand with a MeCN solvent molecule.[21] To understand these experimental results, we must take into account the concentrations of all involved reactants. The standard state concentration of the MeCN solvent is 18.9 M, while the saturated concentration of CO in MeCN is approximately 8 mM.[67] Under the experimental conditions in ref 21, no CO is initially in solution when the electron transfer reaction begins, and the only source of CO is dissociation from **2CO-Re** during the experiment. According to our calculations (Table 6), both **2CO-Re** and **2S-Re** are similarly stable and have equal concentration at [CO] = 1 mM (corresponding to 12.5% CO saturation). At [CO] < 1 mM, the MeCN-bound complex **2S-Re** is more stable and thus CO → MeCN ligand exchange precedes further reduction. These calculations explain the observation of **2S-Re** in the previously described experiment. However, under catalytic conditions, when CO is constantly produced, [CO] > 1 mM (likely closer to 8 mM), and thus ligand exchange between CO and MeCN should be unfavorable. Active catalyst **3-Re** is regenerated following a further one-electron reduction, and dissociation of CO or MeCN occurs (depending on if **2CO** or **2S** is present). For the Mn intermediates, five-coordinate complex **2-Mn** is more stable than **2CO-Mn** or **2S-Mn** under all [CO] = 0−8 mM. Therefore, spontaneous release of CO from **2CO-Mn** to generate **2-Mn** occurs during catalysis. Upon formation of **2-Mn**, this species can dimerize via a radical−radical coupling reaction that we have previously described as extremely rapid, or this species can be reduced by another electron to form active catalyst **3-Mn**. Direct reduction of **2-Mn** should be rapid since we are operating at sufficiently negative potentials during catalysis.

Bonding. Structural parameters for all reaction intermediates in the catalytic cycles are given in Table 7. Since this study focuses on the activation of the CO_2 molecule, we directly compare the bond distances of the bound CO_2 ligand and its products in the various Mn and Re intermediates with the respective structural parameters of an isolated CO_2 molecule and species that form when isolated CO_2 is reduced and protonated. Here, we consider (i) CO_2; (ii) formate

Table 7. Structural Parameters for Reaction Intermediates of the Catalytic Cycle^a

species	C−O$_A$ (Mn/Re)	C−O$_B$ (Mn/Re)	O$_A$−C−O$_B$ (Mn/Re)	M−C (Mn/Re)	C−C (Mn/Re)
3					1.43/1.42
TS **3** → **5**	1.19/1.19	1.19/1.19	152.8/152.8	2.81/2.94	1.44/1.43
5	1.24/1.25	1.24/1.25	130.0/127.6	2.27/2.35	1.47/1.46
6	1.22/1.22	1.37/1.37	117.8/117.8	2.06/2.20	1.48/1.47
7	1.14/1.14			1.88/2.01	1.48/1.47
8	1.22/1.22	1.38/1.38	115.2/114.8	2.07/2.22	1.43/1.42
2CO	1.14/1.14			1.87/2.01	1.43/1.42
CO_2	1.16	1.16	180.0		
HCOO⁻	1.25	1.25	129.2		
HCOOH	1.21	1.33	125.3		
CO	1.13				

^{a}Listed are the relevant distances (Å) and angles (deg) of the CO_2 ligand bound to active catalyst **3** and its reaction products. C−O$_B$ is the carbon−oxygen bond that is cleaved, and C−O$_A$ is the other carbon−oxygen bond that remains after C−O bond cleavage. M−C is the metal−carbon bond of the bound CO_2 molecule, and C−C is the bridging carbon−carbon bond in the bpy ligand. For comparison, bond distances for isolated CO_2 as well as reduction and protonation products are listed.

Table 8. Mulliken Charges for All Reaction Intermediates of the Mn and Re Catalytic Cycles, Consisting of the Sum of the Mulliken Populations of All Atoms Belonging to the Metal (M), the Three CO Ligands ((CO)$_3$), the Metal Tricarbonyl Fragment (M(CO)$_3$), the Bpy Ligand, and the Sixth Ligand (either CO_2^-, COOH, or CO), Respectively

intermediate	M (Mn/Re)	(CO)$_3$ (Mn/Re)	M(CO)$_3$ (Mn/Re)	bpy (Mn/Re)	sixth ligand (Mn/Re)
3	−0.10/0.59	−0.34/−0.92	−0.44/−0.33	−0.56/−0.67	
5	−0.44/0.31	−0.13/−0.89	−0.58/−0.58	−0.01/−0.01	−0.42/−0.40
6	−0.37/0.43	0.08/−0.71	−0.28/−0.28	0.45/0.44	−0.17/−0.16
7	−0.28/0.50	0.41/−0.25	0.13/0.25	0.70/0.68	0.18/0.07
8	−0.44/0.40	−0.05/−0.91	−0.51/−0.50	−0.34/−0.35	−0.16/−0.14
2CO	−0.33/0.52	0.25/−0.45	−0.07/0.07	−0.08/−0.10	0.15/0.03

(HCOO$^-$), which is formed when a hydride (H$^-$) is added to the carbon of CO_2; (iii) formic acid (HCOOH), which is formed upon protonation of HCOO$^-$; and (iv) CO, which is the final product in our study. This comparison allows us to monitor the progress of CO_2 activation by the Mn and Re catalysts at each step in the mechanism. Additionally, we consider the length of the bridging C−C bond between the two pyridine moieties of the bpy ligand as a measure of the amount of electron density on this non-innocent ligand. Previously, studies have shown that a short C−C bond distance (1.40−1.42 Å) indicates that the bpy ligand is reduced by a single electron, i.e., the bpy π^* orbital is occupied, whereas a longer C−C bond (1.46−1.48 Å) indicates that the bpy ligand is unreduced.[15,20,68]

The bond distances in the metal−CO_2 moieties for each intermediate show negligible differences (maximum of 0.01 Å) between the Mn and Re catalysts, with the exception of the metal−carbon distance (Table 8). This agreement indicates that CO_2 activation proceeds in a similar manner for both catalysts. Upon CO_2 binding to the active catalyst 3 (to form 5, see Figure 2), the C−O bond length increases by about 0.1 Å compared to an isolated CO_2 molecule, weakening both C−O double bonds. These C−O bond lengths are similar to the C−O bond lengths in HCOO$^-$, indicating that a significant amount of electron density has already been transferred to the CO_2 ligand at this step in the mechanism. Additionally, for intermediate 5, the bridging C−C bond in the bpy ligand is elongated by 0.04 Å compared to this C−C bond in the active catalyst 3, indicating less charge density in the bpy π^* orbital of intermediate 5, consistent with electron transfer to the CO_2 ligand. The next step in the mechanism, protonation of 5 to yield 6, results in asymmetry between the two C−O bonds. These C−O distances in 6 are similar to those in HCOOH, which formally has one C−O double bond and one C−O single bond (i.e., protonation has further weakened one of the C−O bonds). Proceeding through the reduction-first pathway shown in Figure 4, the addition of one electron to 6 yields 8. This reduction does not notably change the bond lengths in the CO_2 ligand since this reduction is primarily bpy ligand-based. The following protonation step, from 8 → 2CO, as well as the protonation step in the protonation-first pathway (6 → 7), sufficiently weakens the C−OH bond (C−O$_B$) to cleave this C−O$_B$ bond and leave a single CO molecule coordinated to the metal center. In the protonation-first pathway, further reduction of 7 to form 2CO does not affect the C−O$_A$ bond distance. This indicates that, similar to the comparison between 6 and 8, the reducing electron does not affect the resulting CO ligand since this reduction is primarily bpy-based. These ligand-based reductions are reflected in a shortened bridging C−C bond in the bpy ligand for 8 and 2CO (by 0.05 Å). The addition of a second electron to 2CO to regenerate active catalyst 3 does not

alter the bridging C−C bond length in the bpy ligand, suggesting that reduction occurs at the metal center.

Electronic Configuration. In order to gain insight into the overall electronic structure of the intermediates in the catalytic cycles, we have tabulated the Mulliken populations for various moieties of the intermediates in Table 8 as a rough metric. For this analysis, we divide each intermediate into four moieties: (i) the metal center M; (ii) the three CO ligands; (iii) the bpy ligand; and (iv) the sixth ligand (CO_2^-, COOH, or CO). Since metal carbonyl complexes are known to exhibit π-backbonding from the metal center to CO ligands to varying degrees,[69] we include the sum of the Mulliken charges of the metal tricarbonyl (M(CO)$_3$) unit for the various Mn and Re intermediates, as well.

First, we discuss the Mulliken charges for the various intermediates of the Re catalyst. The active catalyst, **3-Re**, with a net charge of −1 has a partially reduced bpy ligand, carrying a negative charge of 0.67 electrons. The Re center in **3-Re** has a net positive charge, while the tricarbonyl fragment carries approximately one extra electron. Upon CO_2 binding to the Re center (to form **5-Re**), the bpy ligand transfers 0.40 electrons to the CO_2 molecule. In this step, the bpy ligand loses 0.66 electrons overall, reducing not only the CO_2 ligand but also transferring 0.28 electrons to the Re center. This electron transfer from the bpy ligand to the Re center enables Re to form a σ bond with the carbon of the CO_2 ligand. Protonation of the CO_2 ligand adds a +1 charge to the complex (to form neutral **6-Re**) and increases the electron affinity of the reduced CO_2 ligand, resulting in the Re(bpy)(CO)$_3$ fragment transferring an additional 0.76 electrons to the COOH ligand. This electron transfer comes from the bpy ligand (0.45 electrons), as well as from the Re(CO)$_3$ moiety (0.30 electrons). As described above, there are two possible pathways for CO_2 reduction: reduction-first and protonation-first (Figure 4). For the reduction-first pathway, reduction of **6-Re** to generate **8-Re** results in minimal change in the charge of the COOH ligand (0.02 electrons). The additional charge from this added electron primarily resides in the bpy ligand (0.79 electrons), with a small contribution (0.22 electrons) residing in the Re(CO)$_3$ moiety. Protonation of **8-Re** to generate **2CO-Re** results in C−O bond cleavage (and loss of H$_2$O), which occurs via the transfer of 0.25 electrons from the bpy ligand, 0.57 electrons from the Re(CO)$_3$ moiety, and 0.17 electrons from charge rearrangements in the sixth ligand. Interestingly, for the protonation-first pathway, a similar amount of charge (0.24 electrons) is transferred from the bpy ligand to cleave the C−O bond (protonation of **6-Re** to generate **7-Re**); however, **6-Re** carries one less electron overall than **8-Re**. The amount of charge transferred by the Re(CO)$_3$ moiety in this step is very similar to the reduction-first pathway (0.53 electrons). Upon reduction of **7-Re** to **2CO-Re**, 0.78 electrons are transferred to

the bpy ligand and 0.18 electrons are transferred to the $Re(CO)_3$ moiety. This amount of electron transfer to each fragment is very similar to the amount of electron transfer in the reduction of **6-Re** to generate **8-Re** in the reduction-first pathway. Finally, for the second reduction step in the catalytic cycle (reduction of **2CO-Re** to regenerate **3-Re**), 0.57 electrons are transferred to the bpy ligand and 0.40 electrons are transferred to the $Re(CO)_3$ moiety. This second reduction leads to the weakening of an axial Re−CO bond, resulting in formation of five-coordinate **3-Re**.

For the Mn catalyst, the trends for charge transfer amongst the analogous fragments in the intermediates of the catalytic cycle are very similar to the trends for the Re catalyst. There are, however, some notable differences. In general, more electron density accumulates on the Mn center than on the Re center in each corresponding intermediate (0.69 to 0.85 electrons more), as expected based on their relative electron affinities (d_{z^2} energy levels) discussed earlier. For the Re catalyst, this trend is primarily balanced by a larger amount of electron density on the three CO ligands. The charge population of the $Re(CO)_3$ and $Mn(CO)_3$ moieties are approximately equal between the corresponding intermediates, except for intermediates with either a fourth CO ligand or no sixth ligand (**7**, **2CO**, and **3**). In these exceptions, approximately 0.11−0.14 additional negative charge resides on the $Mn(CO)_3$ moiety than on the $Re(CO)_3$ moiety. For the active catalyst **3**, less electron density resides on the bpy ligand (0.11 electrons) for **3-Mn** than for **3-Re**. We have already discussed this trend above and have shown that it causes the singly reduced Mn catalyst precursors (**2X** and **2S**) to lose their sixth ligands. Interestingly, upon CO_2 binding to the metal center, these differences in charge density on the $M(CO)_3$ and bpy moieties for Mn and Re no longer appear. The electron distributions of intermediates **5**, **6**, and **8** are very similar for both catalysts. In each catalyst, the d_{z^2} orbital of the metal is primarily involved in σ bonding to the bound CO_2 molecule. This σ bonding causes the d_{z^2} orbital to shift to lower energy, thereby disrupting the orbital mixing between the bpy π^* orbital and the metal d_{z^2} orbital (which plays a role in the charge distribution of the LUMO in five-coordinate **3**). The respective differences in charge distribution among the $M(CO)_3$ and bpy moieties between Mn and Re intermediates (vide supra) are restored after a C−O bond is cleaved. The similarities in charge distribution between the sixth ligand, the bpy ligand, and the $M(CO)_3$ moiety are reflected in the strikingly similar activation barriers for protonation and C−O bond cleavage (**6** → **7** or **8** → **2CO**) for both catalysts. The C−O bond cleavage barriers, as the highest activation barriers, will ultimately determine the turnover frequencies (TOF) of both catalysts, which are of the same order of magnitude.

The bpy ligand was identified previously as a source and sink of electrons during electrocatalysis for the Re system.[20,22] During catalysis, the Mulliken charge residing on the bpy ligand spans a range of −0.67 (**3-Re**) or −0.56 (**3-Mn**) to 0.68 (**7-Re**) or 0.70 (**7-Mn**), a total range of 1.35 or 1.26 electrons for Re or Mn, respectively. This charge range accounts for the majority of the two electrons used for CO_2 reduction in a complete catalytic cycle. As previously mentioned, differences in electron population on the bpy ligand between the Re and Mn catalysts arise only in the five-coordinate complexes (i.e., in active catalyst **3**). In all other intermediates, the charge population on the bpy ligand is nearly identical for both catalysts. Interestingly, the changes in charge population on the bpy

ligand in the C−O bond cleavage steps are nearly identical (0.25 and 0.26 for **6** → **7** and **8** → **2CO**, respectively). Since the net charge in these two steps differs by one electron, the reducing power for these steps comes solely from the bpy ligand, and the reducing electron to generate **8** does not affect the COOH ligand, but only the bpy ligand and the $M(CO)_3$ moiety.

Previous computational work on **3-Mn** showed that it possesses two nearly isoenergetic electronic solutions, a closed-shell singlet solution, and a singlet diradical solution (with one singly occupied molecular orbital (SOMO) on Mn, with mainly d_{z^2} character, and the other SOMO on the bpy ligand, with mainly π^* character (see Supporting Information and Figure S1 for further details).[68,70] We attempted to compute a similar electronic configuration for **3-Re** but instead found only the closed-shell singlet solution. This finding is in agreement with the results from Benson et al., who computed for the same complex the gas phase triplet state to be 0.79 eV higher in energy than the closed-shell singlet state and who found no stable open-shell singlet solution.[26] We also attempted to converge a singlet diradical electronic structure for all other singlet intermediates (**5**, **6**, and **7**). However, their electronic structures always converged to the closed-shell singlet for Re as well as for Mn. For **5-Mn**, **6-Mn**, and **7-Mn**, in contrast to **3-Mn**, the addition of a sixth ligand pushes electron density from the d_{z^2} orbital onto the bpy ligand, preventing a singlet diradical structure from forming.

Microkinetics Simulation. We have described the possible catalytic pathways for the Mn and Re catalysts above. Our calculations indicate that the Re catalyst may prefer a reduction-first pathway and the Mn catalyst may prefer a protonation-first pathway. In both pathways, the C−O bond cleavage steps exhibit the highest activation barriers at different stages and therefore the accumulating intermediates should be different if the two catalysts proceed via different mechanistic pathways. Here, we test this hypothesis by performing microkinetic simulations on the catalytic cycle using all computed reaction free energies, reduction potentials, and activation free energies (reaction rate constants derived from the activation free energies and equilibrium constants for all reactions as well as pK_a values for selected species are tabulated in Tables S2−S4). For this purpose, we developed a Matlab script that incorporates these computed parameters and simulates the reaction course under different operating potentials. From the resulting data, we can monitor the product distribution (selectivity), monitor the accumulating reaction intermediates (mechanistic pathway), and calculate TOFs. Since we are only interested in the electrocatalytic process involving five-coordinate, anionic **3**, we have excluded dimerization in our microkinetics simulation.

To compare simulated and experimental TOF values, we obtained cyclic voltammograms (CVs) of **1-Mn** in CO_2-saturated MeCN with various amounts of added phenol as a H^+ source (see Supporting Information, Figures S2 and S3) and compared these experiments with CVs previously reported by Wong et al. for **1-Re** in CO_2-saturated MeCN with added phenol.[18] Here we use peak catalytic current values (i.e., i_{cat}/i_p values), which are known to directly correlate with catalytic rate constants, in order to derive experimental TOF values. Under CO_2, with 0.20 and 0.57 M phenol (for Mn and Re, respectively), experimental TOF values of 7.2 and 300 s^{-1} are determined for the Mn and Re catalysts, respectively (derived

Table 9. Activation Barriers (kcal/mol) for C−O Bond Cleavage of Neutral and Reduced [Mn(bpy)(CO)₃COOH]⁰/⁻ (6-Mn and 8-Mn) and [Re(bpy)(CO)₃COOH]⁰/⁻ (6-Re and 8-Re)[a]

reaction	$\Delta G\ddagger$ (Mn catalyst)			$\Delta G\ddagger$ (Re catalyst)		
	DFT-B3LYP	ULPNO-CCSD	DLPNO-CCSD(T)	DFT-B3LYP	ULPNO-CCSD	DLPNO-CCSD(T)
6 → 7	11.9	16.6	17.5	11.9	14.3	12.7
8 → 2CO	11.9	16.6		11.6	14.5	

[a]The DFT-B3LYP values are calculated using basis set B2. The CC values are calculated using ma-SVP/ma-TZVP basis set extrapolation and using ZORA. All values are given for standard states at room temperature.

from i_{cat}/i_p = 6.1 and 40 for Mn and Re, respectively, as described in the Supporting Information).

The time-resolved intermediate distribution for each catalytic cycle in our microkinetics simulation was analyzed. Only CO (generation of species **4**, necessary for H₂ generation, was not observed) is generated during this microkinetics simulation. The slopes of the [CO] versus time plots yield TOFs for both catalysts (Figure S4). From these calculations, the Re catalyst has a TOF of 1.1×10^4 s⁻¹ (at an applied potential of −2.0 V vs SCE), and the Mn catalyst has a TOF of 2.5×10^3 s⁻¹ (at −1.7 V vs SCE). The computed TOF values are two orders of magnitude higher than the experimental data presented above, indicating that the calculated activation barriers are probably too low. Previous studies have shown that DFT-B3LYP underestimates activation barriers.[71] For higher accuracy, we calculated CCSD and CCSD(T) activation barriers, using local correlation approximations that have been shown to deviate by less than 1 kcal/mol (on average) compared to conventional nonlocal results.[45−47] These refined activation barriers are given in Table 9. Calculated CCSD(T) values are assumed to be more accurate than CCSD values; however, the former are only available for closed-shell calculations. Our results for the two methods (e.g., for **6 → 7**) differ by only ∼1−1.5 kcal/mol; we therefore use only the calculated ULPNO-CCSD values for microkinetics simulation for consistency across all reactions. The activation barriers are ∼3−5 kcal/mol higher when applying the coupled-cluster method as compared to those calculated with DFT-B3LYP. The microkinetics simulations, with these more accurate activation barriers (see Figure S4 in Supporting Information), result in TOF values of 83 s⁻¹ (at −2.0 V vs SCE) and 0.9 s⁻¹ (at −1.7 V as well as at −2.0 V vs SCE) for the Re and Mn catalysts, respectively. These calculated TOF values are in decent agreement with the experimental data, underestimating them by less than an order of magnitude. These calculations also indicate that the Mn catalyst exhibits a lower TOF due to a higher barrier for C−O bond cleavage as compared to the Re catalyst (Table 9).

Now that an agreement has been established between our model and experimental results, we can make predictions for catalytic pathways and identify accumulating species during catalysis. Figure 6 shows the percentages of all accumulating reaction intermediates at different applied potentials for each catalyst. For the Re catalyst, intermediate **8-Re** accumulates during catalysis at potentials greater than −1.7 V vs SCE. Thus, this catalytic reaction proceeds, as predicted above, via the reduction-first pathway, and the rate-limiting step in this mechanism is proton-coupled C−O bond cleavage. This rate-limiting step is very similar to the rate-limiting step recently identified by Costentin and Savéant in Fe porphyrin electrocatalysts for CO₂ reduction.[72] Below a certain potential (−1.5 V vs SCE), the catalytic reaction cannot proceed when intermediates **2X-Re** and **2CO-Re** begin accumulating. Intermediates **2X-Re** and **2CO-Re** accumulate when mecha-
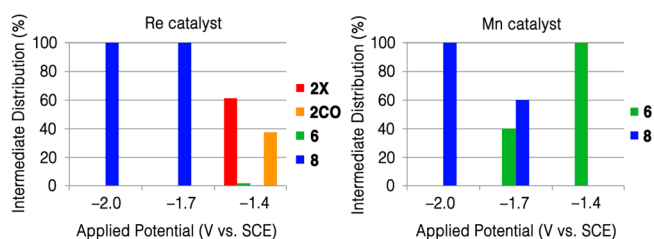

Figure 6. Intermediate distribution at steady state for the Mn and Re catalysts under different reaction conditions. Only intermediates **2X**, **2CO**, **6**, and **8** accumulate in significant concentrations and are shown.

nistic step **2X-Re/2CO-Re → 3-Re** is thermodynamically too costly, and the Cl⁻ or CO ligand cannot dissociate from the Re center. For this Re catalyst, the higher overpotential (as compared to the Mn catalyst) is required to generate the active catalyst **3-Re**. We note that the accumulating species distribution at these precatalytic potentials is strongly dependent on the nature of the sixth ligand of the starting Re complex, as has been shown by multiple experimental studies.[25,61,73] For simplicity, we chose to only study the precatalytic intermediates resulting from the starting **1-Re** complex, which has a Cl⁻ as the sixth ligand.

For the Mn catalyst, at high overpotentials (above −1.8 V vs SCE), intermediate **8-Mn** accumulates during catalysis and the catalytic reaction proceeds via the reduction-first pathway, in a similar fashion to the Re catalyst. However, at lower applied potentials (approximately −1.7 V vs SCE), **8-Mn** and **6-Mn** both accumulate during catalysis and the Mn catalyst proceeds via both the reduction-first and protonation-first pathways. If lower potentials are applied (−1.4 to −1.5 V vs SCE), only intermediate **6-Mn** accumulates during catalysis, and the catalytic reaction solely proceeds via the protonation-first pathway. At all applied potentials for the Mn catalyst, the rate-limiting step is proton-coupled C−O bond cleavage.

These predictions for the differing mechanistic pathways between the Mn and Re catalysts can be experimentally verified. For the Re catalyst, we predict that, at an applied potential of approximately −1.8 V vs SCE, the accumulating intermediate during catalysis is **8-Re**, which is paramagnetic and EPR-active. For the Mn catalyst, at a relatively low applied potential of −1.5 V vs SCE, we predict that the accumulating intermediate during catalysis is **6-Mn**, which is diamagnetic and EPR-silent. At higher applied potentials (greater than −1.8 V vs SCE) for the Mn catalyst, the accumulating intermediate during catalysis is **8-Mn**, which is paramagnetic and EPR-active. In both of these potential regimes for the Mn catalyst, we observe the same catalytic turnover frequencies (0.9 s⁻¹ at −2.0 as well as at −1.5 V vs SCE).

16295

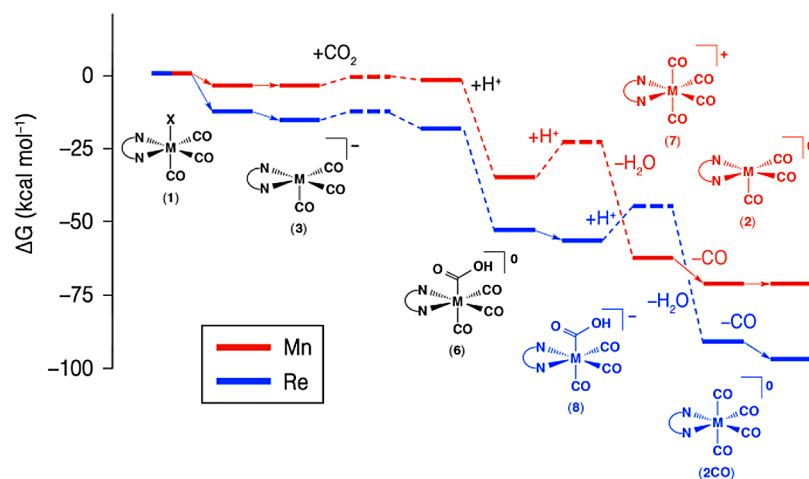dx.doi.org/10.1021/ja508192y | J. Am. Chem. Soc. 2014, 136, 16285−16298

Figure 7. Potential energy surface of the catalytic reaction cycle for the Mn and Re catalysts. Reaction intermediates are depicted with solid lines and transition states with dashed lines. Arrows indicate electron transfer steps. The mechanisms are calculated at the least negative operating potentials for each catalyst (approximately −1.45 and −1.76 V vs SCE for Mn and Re, respectively).

■ CONCLUSIONS

We have performed a computational investigation of electrocatalytic CO_2 reduction by $Mn(bpy)(CO)_3Br$ (**1-Mn**) and $Re(bpy)(CO)_3Cl$ (**1-Re**) and directly compared their catalytic mechanisms. Experimentally, on the electrochemical timescale (100 mV/s), rapid dimerization occurs upon a one-electron reduction of **1-Mn**. In contrast, relatively limited dimerization occurs upon a single-electron reduction of **1-Re**. We demonstrated computationally that upon one-electron reduction **1-Mn** loses Br^- to form a five-coordinate Mn^0 complex that readily dimerizes via barrierless radical−radical coupling. However, one-electron reduction of **1-Re** is primarily bpy ligand-based, and loss of the Cl^- does not occur (formation of **2X-Re**). In order for dimerization to occur, **2X-Re** must lose a Cl^- ligand via a LMCT, which is endergonic by ∼8 kcal/mol. Our analysis shows that binding of a sixth ligand (Cl^- or MeCN) to the one-electron-reduced Re complex **2-Re** is ∼12 kcal/mol more favorable than binding of a sixth ligand to the one-electron-reduced Mn complex **2-Mn**. The observed difference in ligand binding affinity is primarily due to electronic interplay between the metal centers and the bpy ligand. The 5d electrons are bound less strongly to Re than the 3d electrons are bound to Mn. In the reduction of $1 \rightarrow 2$, the added electron is localized more heavily on the bpy ligand in **2-Re**, whereas it is localized more heavily on the metal center in **2-Mn**. The binding of a sixth ligand to **2-Mn** leads to a transfer of electron density from the metal center to the bpy ligand, which is energetically more costly and causes the differences in relative ligand binding energies between **2-Mn** and **2-Re**.

Keith et al. showed for the Re catalyst that selectivity for CO_2 reduction over H^+ reduction originates from a higher barrier for H^+ binding to active catalyst **3-Re** compared to the barrier for CO_2 binding to **3-Re**.[22] The transition state for CO_2 binding to **3-Re** is stabilized by a favorable interaction between the bpy ligand and the CO_2 molecule.[22] We find that the Mn catalyst displays similar selectivity with similar origins as the Re catalyst. However, CO_2 binding to the active Re catalyst **3-Re** is exergonic, whereas CO_2 binding to **3-Mn** is endergonic. CO_2 binding to **3-Mn** becomes thermodynamically favored if it is subsequently protonated from an external weak acid. Experimentally, this difference in the barrier heights for CO_2 binding between Mn and Re helps explain the necessity for an added weak Brønsted acid for catalytic turnover for the Mn catalyst (whereas the Re catalyst operates without an external H^+ source).

We have further identified the mechanistic pathway and performed a microkinetics simulation of the catalytic reaction for each catalyst. Our microkinetics simulation was performed in order to monitor the accumulating intermediates at various applied potentials. The microkinetics simulations indicate the Mn and Re catalysts proceed via two different catalytic mechanisms at their respective minimum operating potentials (−1.45 and −1.76 V vs SCE for Mn and Re), as shown in Figure 7. For both catalysts, the first step in the mechanism is CO_2 binding to the metal center and subsequent protonation of the resulting CO_2 adduct. At this point in the mechanism, more than one electron has already been transferred to the CO_2 ligand, and this electron density was primarily transferred from the bpy ligand. Additionally, one of the C−O bonds has weakened in preparation for C−O bond cleavage. The following steps in the catalytic mechanism depend on the catalyst and on the applied potential.

At an applied potential of −1.4 V vs SCE, **2X-Re** accumulates for the Re catalyst, as the applied potential is not sufficient to generate the active catalyst **3-Re**. However, catalysis can proceed at this applied potential for the Mn catalyst. At −1.4 V vs SCE, a protonation-first pathway is accessed, in which C−O bond cleavage proceeds via the addition of a second H^+ to the −OH group in **6-Mn** (to form water and **7-Mn**). Cationic, tetracarbonyl **7-Mn** is then reduced by another electron and loses an axial CO ligand to generate **2-Mn** (which is further reduced to regenerate active catalyst **3-Mn**). For the Re catalyst an applied potential of −1.76 V vs SCE is necessary to drive the reduction of **2X** to **3** forward. This higher overpotential compared to Mn is necessary due to the Re catalyst's higher binding affinity to a sixth ligand. At −1.8 V vs SCE, both the Mn and Re catalysts proceed via the same catalytic mechanism (reduction-first pathway). After CO_2 binding to **3** and subsequent protonation, resulting intermediate **6** is reduced via a bpy ligand-based reduction to form **8**. Protonation of **8** at the −OH group initiates C−O bond cleavage, resulting in formation of either $[Mn(bpy)(CO)_3]^0$ (**2-Mn**) and release of CO or $[Re(bpy)(CO)_4]^0$ (**2CO-Re**), respectively. **2CO-Re** can undergo ligand exchange with a MeCN solvent molecule (and

Article

subsequent CO release) at low CO concentrations ([CO] < 1 mM). An additional one-electron reduction of these resulting intermediates regenerates active catalyst **3**.

Throughout each catalytic cycle, the bpy ligand exhibits a remarkable redox capability. The addition of electrons to many of the intermediates in each catalytic cycle does not directly reduce the CO_2 ligand, but rather the electron density resides in the bpy ligand. In the course of the catalytic cycle, the bpy ligand transfers electron density to the CO_2 ligand, enabling C–O bond cleavage. This process can be regarded as "charging the bpy ligand." Accumulated electron density on the bpy ligand in active catalyst **3** is necessary to bind CO_2, concomitantly with H^+ addition. Upon binding, the CO_2 ligand is mainly reduced by the electron density from the bpy ligand. The process of charging the bpy ligand is also necessary to release the generated CO product from the metal center, and therefore, this process is necessary to regenerate active catalyst **3** for further CO_2 binding.

The flexibility of the Mn catalyst to access both the protonation-first and reduction-first pathways provides promise for developing new Mn catalysts that operate at significantly lower overpotentials. The Re catalyst's inability to operate via the protonation-first pathway severely limits the available operating potentials for this catalyst system. Additionally, elucidating the mechanism of CO_2 reduction by these Mn and Re catalysts provides insights into how to best increase catalytic rates, namely, by accelerating the rate of proton-coupled C–OH bond cleavage in the relevant intermediates in each mechanistic pathway.

In order to further advance homogeneous catalysts for CO_2 reduction, we have developed design principles based on our computational analysis. The electron affinity of the bpy ligand, or a similar non-innocent ligand, must be high enough to have sufficient reducing power to bind and reduce the CO_2 ligand. Experiments have shown that a variety of substitutions on the bpy ligand can influence the required applied potential for CO_2 reduction and have shown that electron-withdrawing substituents lower the reducing power of the bpy ligand, which shuts off catalysis.[16,74] To further reduce overpotentials for these catalysts, more electron density needs to be located in the metal d_{z^2} orbital in singly reduced, five-coordinate **2**, which in turn lowers the binding affinity for a sixth ligand and leads to more facile CO release in the catalytic cycle. The extent of metal-based reduction to form **2** can be determined by the metal center and the electron affinity of the bpy ligand (or similar non-innocent ligand), as well as other factors. Future computational studies underway include investigating various substitution patterns on the bpy ligand, as well as understanding the effects of various H^+ donors on catalysis.

ASSOCIATED CONTENT

Ⓢ Supporting Information

Computational information is provided on relative reaction rates for dimerization, ligand binding affinities to $[Re(CO)_5]^0$ and $[Mn(CO)_5]^0$, the electronic structure of $[Mn(bpy)-(CO)_3]^0$, product formation during microkinetics simulations, and absolute energies and the coordinates of atoms in all optimized molecules; experimental information is provided on cyclic voltammetry and calculations of TOF values. This material is available free of charge via the Internet at http://pubs.acs.org.

AUTHOR INFORMATION

Corresponding Author
*eac@princeton.edu.
Notes
The authors declare no competing financial interest.

ACKNOWLEDGMENTS

REFERENCES

(1) http://acee.princeton.edu/distillates/.
(2) Simon, P.; Gogotsi, Y.; Dunn, B. *Science* **2014**, *343*, 1210.
(3) Inglis, J. L.; MacLean, B. J.; Pryce, M. T.; Vos, J. G. *Coord. Chem. Rev.* **2012**, *256*, 2571.
(4) Kuhl, K. P.; Cave, E. R.; Abram, D. N.; Jaramillo, T. F. *Energy Environ. Sci.* **2012**, *5*, 7050.
(5) Benson, E. E.; Kubiak, C. P.; Sathrum, A. J.; Smieja, J. M. *Chem. Soc. Rev.* **2009**, *38*, 89.
(6) Kumar, B.; Llorente, M.; Froehlich, J.; Dang, T.; Sathrum, A.; Kubiak, C. P. *Annu. Rev. Phys. Chem.* **2012**, *63*, 541.
(7) Hori, Y. In *Modern Aspects of Electrochemistry*; Vayenas, C., White, R., Gamboa-Aldeco, M., Eds.; Springer: New York, 2008; Vol. 42, p 89.
(8) Qiao, J.; Liu, Y.; Hong, F.; Zhang, J. *Chem. Soc. Rev.* **2014**, *43*, 631.
(9) Windle, C. D.; Perutz, R. N. *Coord. Chem. Rev.* **2012**, *256*, 2562.
(10) Costentin, C.; Robert, M.; Saveant, J.-M. *Chem. Soc. Rev.* **2013**, *42*, 2423.
(11) Kondratenko, E. V.; Mul, G.; Baltrusaitis, J.; Larrazabal, G. O.; Perez-Ramirez, J. *Energy Environ. Sci.* **2013**, *6*, 3112.
(12) Appel, A. M.; Bercaw, J. E.; Bocarsly, A. B.; Dobbek, H.; DuBois, D. L.; Dupuis, M.; Ferry, J. G.; Fujita, E.; Hille, R.; Kenis, P. J. A.; Kerfeld, C. A.; Morris, R. H.; Peden, C. H. F.; Portis, A. R.; Ragsdale, S. W.; Rauchfuss, T. B.; Reek, J. N. H.; Seefeldt, L. C.; Thauer, R. K.; Waldrop, G. L. *Chem. Rev.* **2013**, *113*, 6621.
(13) Grice, K. A.; Kubiak, C. P. In *Advances in Inorganic Chemistry*; Aresta, M, van Eldik, R., Eds.; Academic Press: New York, 2014; Vol. 66, p 163.
(14) Froehlich, J. D.; Kubiak, C. P. *Inorg. Chem.* **2012**, *51*, 3932.
(15) Smieja, J. M.; Benson, E. E.; Kumar, B.; Grice, K. A.; Seu, C. S.; Miller, A. J. M.; Mayer, J. M.; Kubiak, C. P. *Proc. Natl. Acad. Sci. U.S.A.* **2012**, *109*, 15646.
(16) Smieja, J. M.; Kubiak, C. P. *Inorg. Chem.* **2010**, *49*, 9283.
(17) Hawecker, J.; Lehn, J. M.; Ziessel, R. *J. Chem. Soc., Chem. Commun.* **1984**, 328.
(18) Wong, K.-Y.; Chung, W.-H.; Lau, C.-P. *J. Electroanal. Chem.* **1998**, *453*, 161.
(19) Benson, E. E.; Kubiak, C. P. *Chem. Commun.* **2012**, *48*, 7374.
(20) Smieja, J. M.; Sampson, M. D.; Grice, K. A.; Benson, E. E.; Froehlich, J. D.; Kubiak, C. P. *Inorg. Chem.* **2013**, *52*, 2484.
(21) Grice, K. A.; Gu, N. X.; Sampson, M. D.; Kubiak, C. P. *Dalton Trans.* **2013**, *42*, 8498.
(22) Keith, J. A.; Grice, K. A.; Kubiak, C. P.; Carter, E. A. *J. Am. Chem. Soc.* **2013**, *135*, 15823.
(23) Machan, C. W.; Sampson, M. D.; Chabolla, S. A.; Dang, T.; Kubiak, C. P. *Organometallics* **2014**, *33*, 4550.
(24) Grice, K. A.; Gu, N. X.; Sampson, M. D.; Kubiak, C. P. *J. Chem. Soc., Dalton Trans.* **2013**, *42*, 8498.
(25) Johnson, F. P. A.; George, M. W.; Hartl, F.; Turner, J. J. *Organometallics* **1996**, *15*, 3374.
(26) Benson, E. E.; Sampson, M. D.; Grice, K. A.; Smieja, J. M.; Froehlich, J. D.; Friebel, D.; Keith, J. A.; Carter, E. A.; Nilsson, A.; Kubiak, C. P. *Angew. Chem., Int. Ed.* **2013**, *52*, 4841.
(27) *CRC Handbook of Chemistry and Physics*, 92nd ed.; Haynes, W. M., Ed.; CRC Press: Boca Raton, FL, 2011.

(28) Bourrez, M.; Molton, F.; Chardon-Noblat, S.; Deronzier, A. *Angew. Chem., Int. Ed.* **2011**, *50*, 9903.

(29) Sampson, M. D.; Nguyen, A. D.; Grice, K. A.; Moore, C. E.; Rheingold, A. L.; Kubiak, C. P. *J. Am. Chem. Soc.* **2014**, *136*, 5460.

(30) Bourrez, M.; Orio, M.; Molton, F.; Vezin, H.; Duboc, C.; Deronzier, A.; Chardon-Noblat, S. *Angew. Chem., Int. Ed.* **2014**, *53*, 240.

(31) Neese, F. *Wiley Interdiscip. Rev.: Comput. Mol. Sci.* **2012**, *2*, 73.

(32) Becke, A. D. *Phys. Rev. A* **1988**, *38*, 3098.

(33) Becke, A. D. *J. Chem. Phys.* **1993**, *98*, 5648.

(34) Lee, C.; Yang, W.; Parr, R. G. *Phys. Rev. B* **1988**, *37*, 785.

(35) Neese, F.; Wennmohs, F.; Hansen, A.; Becker, U. *Chem. Phys.* **2009**, *356*, 98.

(36) Schäfer, A.; Horn, H.; Ahlrichs, R. *J. Chem. Phys.* **1992**, *97*, 2571.

(37) Weigend, F.; Ahlrichs, R. *Phys. Chem. Chem. Phys.* **2005**, *7*, 3297.

(38) Hay, P. J.; Wadt, W. R. *J. Chem. Phys.* **1985**, *82*, 299.

(39) Dunning, T. H. *J. Chem. Phys.* **1989**, *90*, 1007.

(40) Grimme, S.; Antony, J.; Ehrlich, S.; Krieg, H. *J. Chem. Phys.* **2010**, *132*.

(41) Klamt, A.; Schüürmann, G. *J. Chem. Soc., Perkin Trans. 2* **1993**, 799.

(42) Scott, A. P.; Radom, L. *J. Phys. Chem.* **1996**, *100*, 16502.

(43) Keith, J. A.; Carter, E. A. *J. Chem. Theory Comput.* **2012**, *8*, 3187.

(44) Kelly, C. P.; Cramer, C. J.; Truhlar, D. G. *J. Phys. Chem. B* **2007**, *111*, 408.

(45) Riplinger, C.; Neese, F. *J. Chem. Phys.* **2013**, *138*.

(46) Riplinger, C.; Sandhoefer, B.; Hansen, A.; Neese, F. *J. Chem. Phys.* **2013**, *139*.

(47) Hansen, A.; Liakos, D. G.; Neese, F. *J. Chem. Phys.* **2011**, *135*.

(48) Zheng, J.; Xu, X.; Truhlar, D. *Theor. Chem. Acc.* **2011**, *128*, 295.

(49) Pantazis, D. A.; Chen, X. Y.; Landis, C. R.; Neese, F. *J. Chem. Theory Comput.* **2008**, *4*, 908.

(50) Truhlar, D. G. *Chem. Phys. Lett.* **1998**, *294*, 45.

(51) van Lenthe, E.; Baerends, E. J.; Snijders, J. G. *J. Chem. Phys.* **1994**, *101*, 9783.

(52) van Lenthe, E.; Snijders, J. G.; Baerends, E. J. *J. Chem. Phys.* **1996**, *105*, 6505.

(53) Isse, A. A.; Gennaro, A. *J. Phys. Chem. B* **2010**, *114*, 7894.

(54) Fawcett, W. R. *Liquids, Solutions, and Interfaces: From Classical Macroscopic Descriptions to Modern Microscopic Details*; Oxford University Press: New York, 2004.

(55) Fernández-Ramos, A.; Miller, J. A.; Klippenstein, S. J.; Truhlar, D. G. *Chem. Rev.* **2006**, *106*, 4518.

(56) Pavlishchuk, V. V.; Addison, A. W. *Inorg. Chim. Acta* **2000**, *298*, 97.

(57) Sullivan, B. P.; Bolinger, C. M.; Conrad, D.; Vining, W. J.; Meyer, T. J. *J. Chem. Soc., Chem. Commun.* **1985**, 1414.

(58) Hayashi, Y.; Kita, S.; Brunschwig, B. S.; Fujita, E. *J. Am. Chem. Soc.* **2003**, *125*, 11976.

(59) Grills, D. C.; Farrington, J. A.; Layne, B. H.; Lymar, S. V.; Mello, B. A.; Preses, J. M.; Wishart, J. F. *J. Am. Chem. Soc.* **2014**, *136*, 5563.

(60) Takeda, H.; Koizumi, H.; Okamoto, K.; Ishitani, O. *Chem. Commun.* **2014**, *50*, 1491.

(61) Scheiring, T.; Klein, A.; Kaim, W. *J. Chem. Soc., Perkin Trans. 2* **1997**, 2569.

(62) Fujita, E.; Muckerman, J. T. *Inorg. Chem.* **2004**, *43*, 7636.

(63) Rossenaar, B. D.; Hartl, F.; Stufkens, D. J. *Inorg. Chem.* **1996**, *35*, 6194.

(64) Rossenaar, B. D.; Hartl, F.; Stufkens, D. J.; Amatore, C.; Maisonhaute, E.; Verpeaux, J.-N. *Organometallics* **1997**, *16*, 4675.

(65) Slater, S.; Wagenknecht, J. H. *J. Am. Chem. Soc.* **1984**, *106*, 5367.

(66) Bolinger, C. M.; Sullivan, B. P.; Conrad, D.; Gilbert, J. A.; Story, N.; Meyer, T. J. *J. Chem. Soc., Chem. Commun.* **1985**, 796.

(67) Fujita, E.; Creutz, C.; Sutin, N.; Szalda, D. J. *J. Am. Chem. Soc.* **1991**, *113*, 343.

(68) Scarborough, C. C.; Wieghardt, K. *Inorg. Chem.* **2011**, *50*, 9773.

(69) Hocking, R. K.; Hambley, T. W. *Organometallics* **2007**, *26*, 2815.

(70) Hartl, F.; Rosa, P.; Ricard, L.; Le Floch, P.; Záliš, S. *Coord. Chem. Rev.* **2007**, *251*, 557.

(71) Lynch, B. J.; Truhlar, D. G. *J. Phys. Chem. A* **2001**, *105*, 2936.

(72) Costentin, C.; Drouet, S.; Passard, G.; Robert, M.; Savéant, J.-M. *J. Am. Chem. Soc.* **2013**, *135*, 9023.

(73) Paolucci, F.; Marcaccio, M.; Paradisi, C.; Roffia, S.; Bignozzi, C. A.; Amatore, C. *J. Phys. Chem. B* **1998**, *102*, 4759.

(74) Benson, E. E.; Grice, K. A.; Smieja, J. M.; Kubiak, C. P. *Polyhedron* **2013**, *58*, 229.